Progress In Electromagnetics Research, Vol. 176, 11–23, 2023

Optically Transparent and Mechanically Flexible Coplanar Waveguide-Fed Wideband Antenna Based on Sub-Micron Thick Micro-Metallic Meshes

Jing Pan[1, †], Yuanqing Yao[1, †], Liu Yang[1, 2, *], Hui Li[3], and Sailing He[1, 2, 4, *]

Abstract—An optically transparent and flexible coplanar waveguide (CPW)-fed wideband antenna is proposed and demonstrated experimentally based on sub-micron thick micro-metallic meshes (μ-MMs). Due to the high visible transmittance (83.1%) and low sheet resistance (1.75 Ω/sq) of the silver μ-MM with thickness of only 190 nm, the transparent CPW has very low insertion loss and provides a good feed to the high-performance transparent antenna. The measured S_{11} spectrum of our antenna matches well with that of the opaque counterpart. The measured fractional bandwidth is 22% from 3.4 to 4.25 GHz. Based on numerical modeling, whose accuracy is experimentally verified, the radiation efficiency and peak gain of our transparent antenna at 3.45 GHz are calculated to be 89.7% and 3.03 dBi, respectively. Besides the good optical and electromagnetic properties, our transparent antenna is also highly flexible. Despite the sub-micron thick μ-MMs, the transparency, radiation efficiency, and mechanical properties of our transparent antenna are obviously superior to those of the transparent antennas reported previously, and the overall size and radiation gain are also comparable. Therefore, our transparent antenna has an excellent comprehensive performance, showing great potential for practical applications as well as the emerging applications in the field of flexible and wearable electronics.

1. INTRODUCTION

Transparent antennas are visibly transparent devices that can transmit and receive electromagnetic (EM) signals. Since NASA proposed the first optically transparent microstrip patch antenna in 1997 [1], transparent antennas have experienced great development in the past two decades [2–4]. Because of the see-through feature, transparent antennas can be integrated onto solar panels, satellite, windscreens of automobiles, displays, windows, and so on [2–4], whose intrinsic performances are maintained without much degradation by the antennas. Mechanical flexibility will endow transparent antennas with broader application scenarios, e.g., attachment onto curved surfaces and wearable devices, which however has not been investigated extensively [2, 3].

Transparent conductive films (TCFs) dominate transparent antennas. Up to now, various TCFs have been employed to fabricate transparent antennas. Transparent conductive oxide (TCO) based antennas always have low radiation efficiency and low gain because of the high resistance induced high ohmic loss [5–8]. Indium tin oxide (ITO) is the most popular TCO for transparent antennas [5–7], but is increasingly expensive due to the scarce element of indium. Indium-free TCOs, e.g., fluorine-doped tin oxide (FTO) [5, 7] and gallium-doped zinc oxide [8], have been developed but suffer from the same issue

Received 15 September 2022, Accepted 27 October 2022, Scheduled 31 October 2022

* Corresponding author: Liu Yang (optyang@zju.edu.cn), Sailing He (sailing@zju.edu.cn).

† Jing Pan and Yuanqing Yao contributed equally to this work.

[1] Center for Optical and Electromagnetic Research, National Engineering Research Center for Optical Instruments, College of Optical Science and Engineering, Zhejiang University, Hangzhou 310058, China. [2] Ningbo Research Institute, Zhejiang University, Ningbo 315100, China. [3] School of Information and Communication Engineering, Dalian University of Technology, Dalian 116024, China. [4] JORCEP, School of Electrical Engineering, Royal Institute of Technology (KTH), S-100 44 Stockholm, Sweden.

with ITO, that is brittleness [9]. Hybridizing sub-10-nm thick metals with one- or two-layer TCO can form multilayer TCFs with increased conductivity but decreased transparency [10–12]. Silver-coated polyester (AgHT), consisting of a TCO/Ag/TCO multilayer coating on a flexible polyethylene glycol terephthalate (PET) substrate, has similar optical and electrical properties to multilayer TCFs [13–15]. But the thick TCO layers are unfriendly to the mechanical flexibility, and bending tests have not been reported for the AgHT-based transparent antennas [13–15]. Carbon-based materials, e.g., conductive polymers [16, 17], graphene [18–21], and carbon nanotubes (CNTs) [22], have been reported for transparent and flexible antennas. However, due to the high resistances of the transparent thin films, the radiation properties of the antennas cannot compete with those of the TCO-based antennas [5–8]. Metallic nanowire (NW) networks can be made more conductive with higher densities of NWsfor high-efficiency antennas, which however have poorer optical transparency [23–27].

Metallic mesh (MM) based TCFs have also been widely applied in high-efficiency and high-gain transparent antennas because the optical transparency and the electrical conductivity can be well balanced at a higher level [11, 28–38]. There are two types of MMs: one is wired MM [28–30]; the other is micro-MM or μ-MM [11, 30–38]. In wired MM, metallic wires are woven together and loosely connected at the wire junctions, while in μ-MM, the mesh lines are self-connected and do not have serious junction resistances that exist in wired MM. Therefore, μ-MM is more attractive. Silver (Ag), copper, gold, nickel, and metallic alloys have been reported to fabricate MMs. Note that they are always made very thick, several micrometers [11, 31–33, 36–38] or even up to a hundred micrometer [34], in order to reduce skin depth loss of the MM-based antennas. Thick antennas inevitably use more materials and have high cost, especially when the expensive gold is used [32, 34]. Meanwhile, too thick MM, e.g., the 100-μm thick MM [34], will also be likely to introduce optical shadows, affecting visual experience of human from different angles.

Here in this work, we experimentally demonstrate an optically transparent and mechanically flexible antenna based on sub-micron thick Ag μ-MMs. It will be the thinnest MM-based transparent antenna. Our antenna consists of a fan-shaped patch fed with a coplanar waveguide (CPW), working in a wide band of 3.4–4.25 GHz. The single-layer design allows a high optical transmittance up to 83.1%. Though the μ-MM is only sub-micron thick, its sheet resistance (R_{sh}) still keeps very small, i.e., 1.75 Ω/sq, allowing for high radiation efficiency and high gain, comparable and even superior to those of the reported transparent antennas based on μ-MMs with micron thicknesses [11, 31–33, 36–38]. Besides, our antenna also shows very good mechanical flexibility, and is potentially applied to the emerging field of flexible and wearable electronics. By appropriate optimization, our antenna may also be used to receive EM signals or even higher frequency signals for detection [39–45].

2. DESIGN, SIMULATION AND EXPERIMENTS

2.1. Design and Simulation

A monopole antenna can be obtained from planarization of a cylindrical element antenna. If the cylinder height and radius are L and r, respectively, the equivalent monopole patch width and length can be $W = 2\pi r$ and $H \approx L$, respectively. According to the cylindrical element approximation method, the lower frequency limit, f_L, of the patch antenna can be estimated with the empirical formula below:

$$f_L = \frac{c}{\lambda_L} = \frac{72}{L + r}, \tag{1}$$

where c is the light speed in vacuum, and λ_L is the light wavelength. Since a fan-shaped patch can be transformed geometrically from the square patch with the same size, its lowest frequency can also be estimated as f_L, as expressed in Eq. (1). When we set $W = H = 30$ mm, f_L is about 2.1 GHz. On the other hand, the radiation bandwidth can be widened by the fan-shaped patch, which can be regarded as a uniformly tapered transmission line, allowing impedance matching over a wide bandwidth. Therefore, we propose and design a sectorial monopole wideband antenna fed with a CPW, as schematically shown in Fig. 1(a). The CPW makes the antenna easy to integrate and realize miniaturization. Such a single-layer design is also favorable for optical transparency. The electromagnetic (EM) properties of the CPW are investigated individually as shown in Fig. 1(b). To make them transparent and flexible, both the antenna and CPW are composed of Ag μ-MM on top of a piece of polyethene (PE) substrate with

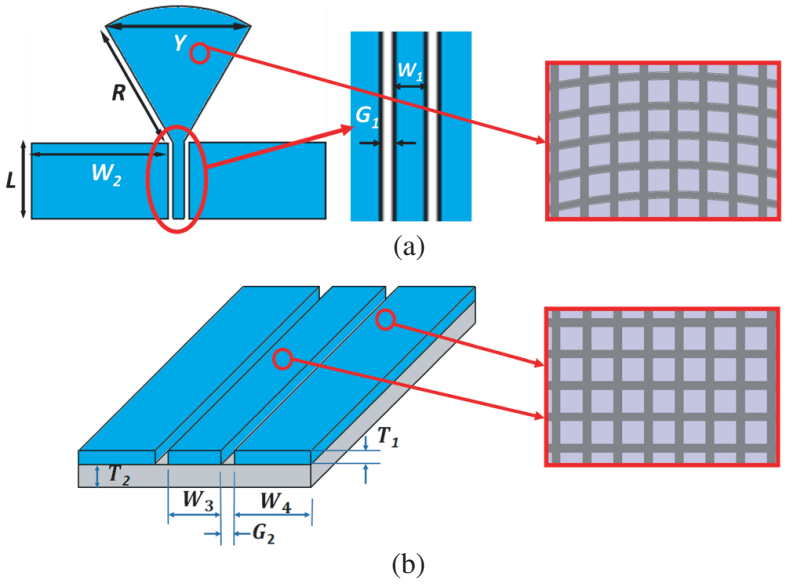

Figure 1. Schematic diagrams of (a) our antenna and (b) CPW based on Ag μ-MM.

thickness of 50 μm, dielectric constant of 2.3, and loss tangent of 0.00031. The grids in the fan-shaped patch region also have sectorial shapes, as shown in the inset of Fig. 1(a); while the grids in the CPW region are rectangular, as shown in the inset of Fig. 1(b). Their opening ratios (ORs), which determine the areal optical transparency, are kept almost the same so that the antenna looks transparent uniformly. Main geometrical parameters are listed in Table 1, allowing us to achieve a resonance around 4 GHz (to be demonstrated in the next Section). The wideband antenna has a high degree of tolerance to the size of the CPW gap. Therefore, we set a smaller gap size for the CPW when it is studied individually.

Table 1. Main geometrical parameters of our antenna and CPW.

Parameter	Size (mm)	Parameter	Size (μm)
Y	29.8	T_1	0.19
R	27.9	T_2	50
W_1	2	G_2	160
W_2	28.5	W_3	2000
L	15.635	W_4	8000
G_1	0.45		

Numerical simulations were performed using CST Microwave Studio, where the Ag μ-MM were treated as a complete film for the convenience of modeling. In the numerical simulation, the conductivity (σ) of the equivalent film is set to a value taken from the measured sheet resistance, R_{sh}, of the fabricated Ag μ-MM with thickness of T_1 using the following equation:

$$\sigma = \frac{1}{R_{sh} \cdot T_1}. \tag{2}$$

Such a simplified simulation method is reasonable, because the simulated result well matches the measured EM property. Our fabricated antennas based on μ-MM and the solid film also have very close radiation performances, confirming again the negligible scattering effect of the Ag grids (to be demonstrated in detail in the next Section).

2.2. Fabrication

Our transparent antenna and CPW were fabricated on PE substrates, which were rinsed ultrasonically in acetone, isopropanol, and deionized water in sequence, each for 10 min. On the clean substrate, a layer of photoresist (PR; AZ5214) with thickness about 1.2 μm was spin-coated at 6000 rpm for 59 s. After ultraviolet photolithography, the pre-designed pattern in the photomask was transferred to the PR. Then, Ag was deposited at a rate of 0.46 Å/s with a magnetron sputter (Kurt J Lesker PVD75; DC power: 100 W, argon pressure: 3 mTorr, room temperature). Finally, a lift-off process was carried out by immersing the sample into acetone to remove PR and the Ag on top of it. The Ag directly on the substrate remained as our fabricated devices. For comparison, an opaque antenna consisting of solid Ag films with the same thickness was also fabricated.

2.3. Characterization

The S-parameters of the fabricated CPWs and antennas were measured by a vector network analyzer (VNA; Rohde & Schwarz ZVA 40). To minimize the coupling loss, we used conductive Ag paste to adhere sub-miniature A (SMA) connectors to the devices. For flexibility tests, CPWs and antennas were bent for 500 cycles with a fixed curvature radius of about 6 mm. To quantitatively characterize the optical and electrical properties of the Ag μ-MM, on which the antenna and CPW were built, we fabricated Ag μ-MM (6 mm × 6 mm) between two Ag pads on a piece of 2 cm × 2 cm quartz with the above processes. A microspectrophotometer was employed to measure the optical transmittance of the μ-MM in the visible wavelength range, which was normalized to the transmittance of the substrate. Its R_{sh} was measured with a sourcemeter (Keithley 2450) through two probes connecting to the Ag pads on the two sides.

3. RESULTS AND DISCUSSION

3.1. Silver μ-MM with High Transparency and High Conductivity

Before investigating transparent antenna and CPW, it is of great necessity to first study the properties of the component Ag μ-MM. Fig. 2(a) shows a photo of a 6 mm × 6 mm Ag μ-MM between Ag pads at two sides fabricated on quartz. The mesh line width is 10 μm, and the period, p, of both 100 and 150 μm are considered for dense and sparse meshes, respectively. The opening ratios (ORs) of those meshes are 81% and 87.1%, respectively. To study the effect of the mesh thickness, t, on the optical and electrical properties, Ag μ-MMs with different t values were fabricated and characterized.

Figures 2(b) and 2(c) show the measured transmittance spectra as functions of thickness for the dense and sparse Ag μ-MMs, respectively. For both cases with different mesh periods, as t increases, optical transmittances decrease to their ORs approximately and become less sensitive to the light wavelength. This indicates that the thin mesh lines with wavelength-dependent transmittances become opaque when $t > 50$ nm and in this case, only the Ag-absent spacing between the opaque lines determines the optical transmission. Therefore, even the 237-nm thickest meshes still show average transmittances above 80%, i.e., $\sim 82.5\%$ and $\sim 88\%$ for the μ-MMs with $p = 100$ and 150 μm, respectively. They are relatively larger than their ORs, probably induced by the testing error of the microspectrophotometer, from which a little bit higher transmittance is always measured. Neglecting the errors, the good optical properties mean highly transparent antennas and CPWs based on these Ag μ-MMs.

On the other hand, in Fig. 2(d), the measured R_{sh} of the Ag μ-MM drops quickly when t increases from 14 nm to 53 nm, and then slowly when further increasing t to 237 nm, no matter what the mesh period is. The R_{sh} values of the μ-MMs with $t = 190$ and 237 nm are very close to each other. This indicates that the 190-nm thick μ-MM is sufficiently thick to mitigate the surface scattering of carriers that is the main reason for the high resistance of thin meshes. Because of more carrier transportation paths, the dense μ-MM with $p = 100$ μm is more conductive than the sparse one with $p = 150$ μm (Fig. 2(d)).

Figure 2(e) shows average transmittance in the wavelength range of 400–800 nm, T_{ave}, versus R_{sh} of four most conductive Ag μ-MMs with $t = 237$ and 190 nm, and $p = 100$ and 150 μm, respectively. For

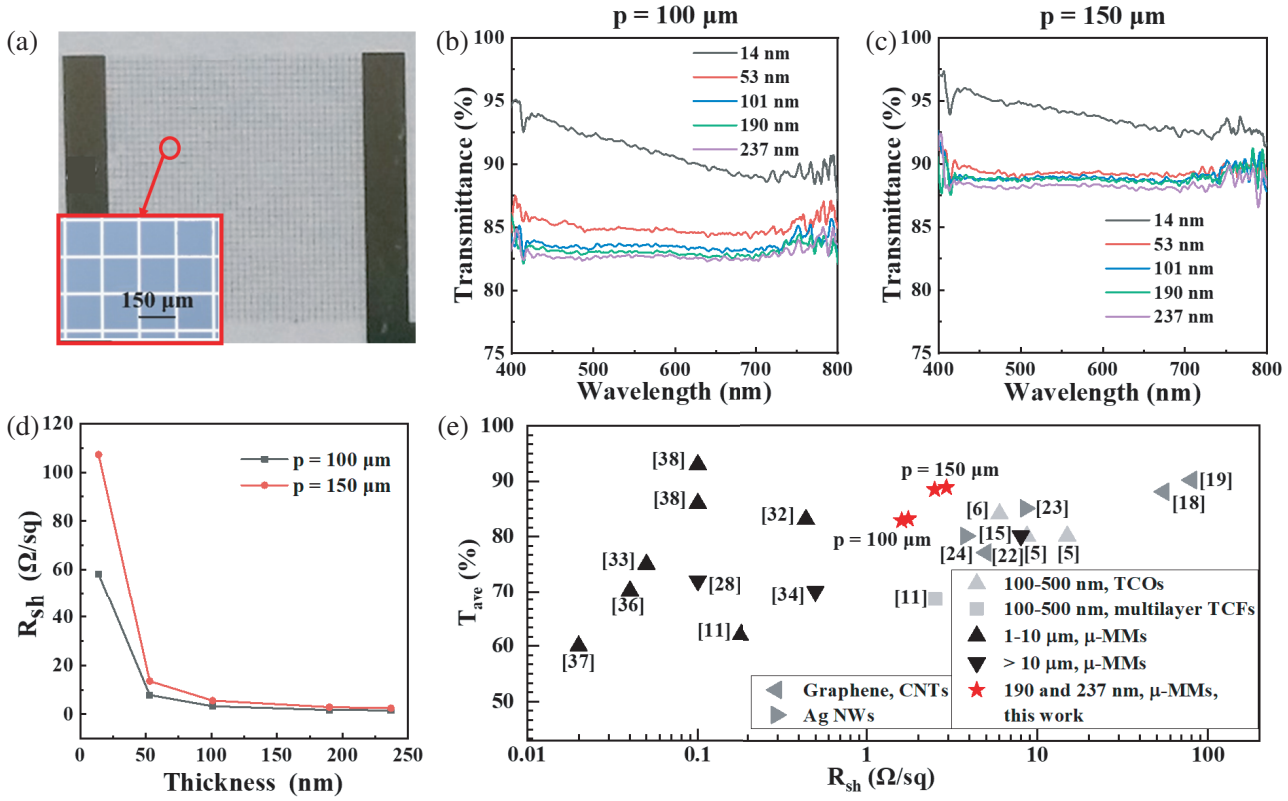

Figure 2. (a) Photograph of our fabricated Ag µ-MM between two Ag pads on quartz. Measured transmittance spectra as functions of thicknesses for Ag µ-MMs with different grid periods, namely, (b) $p = 100\,\mu m$ and (c) $p = 150\,\mu m$, as well as (d) their sheet resistances, R_{sh}. (e) Average transmittance in the wavelength range of 400–800 nm, T_{ave}, versus R_{sh} for four most conductive Ag µ-MMs ($t = 190$ and 237 nm, $p = 100$ and 150 µm) and previously-reported representative TCFs used for transparent antennas [5, 6, 11, 15, 18, 19, 22–24, 28, 32–34, 36–38].

comparison, T_{ave} vs R_{sh} for representative TCFs used for transparent antennas [5, 6, 11, 15, 18, 19, 22–24, 28, 32–34, 36–38] are also plotted. It is seen that R_{sh}'s of our sub-micron Ag µ-MMs are between those of very thick MMs and those of TCFs based on TCOs, multilayer TCFs, AgHTs as well as graphene, CNTs and Ag NW networks, while with less metallic absorption, the transmittances of our Ag µ-MMs are among top 10 highest values of all TCFs in comparison in Fig. 2(e). It means that good optical and electrical properties are achieved by our Ag µ-MMs with far less thickness than 1 µm, which are promising to form transparent CPW and antenna with satisfied overall performances to be demonstrated below.

3.2. Transparent CPW and Transparent Antenna

As aforementioned, transparent CPW for feeding the antenna is first presented. Based on transparent Ag µ-MMs with $t = 190$ nm and $p = 100$ and 150 µm, CPWs with different lengths (i.e., $L = 25$, 50, 75 mm) were fabricated and characterized. One CPW sample with $p = 100\,\mu m$ and $L = 25$ mm is demonstrated in the inset of Fig. 3(c). Due to the fact that visible light can transmit through the µ-MM without much loss, the university logs under the CPW are clearly seen, showing very good visible transparency. The measured S_{21} spectra were plotted in Figs. 3(a) and 3(b) for CPWs with sparse and dense Ag µ-MMs, respectively. For each sample, S_{21} decreases as the frequency increases and the trend can be approximated with a linear line, as expected. This means that the insertion losses of the CPWs increase almost linearly with the increasing frequency. For lengths of 25, 50 and 75 cm, the insertion

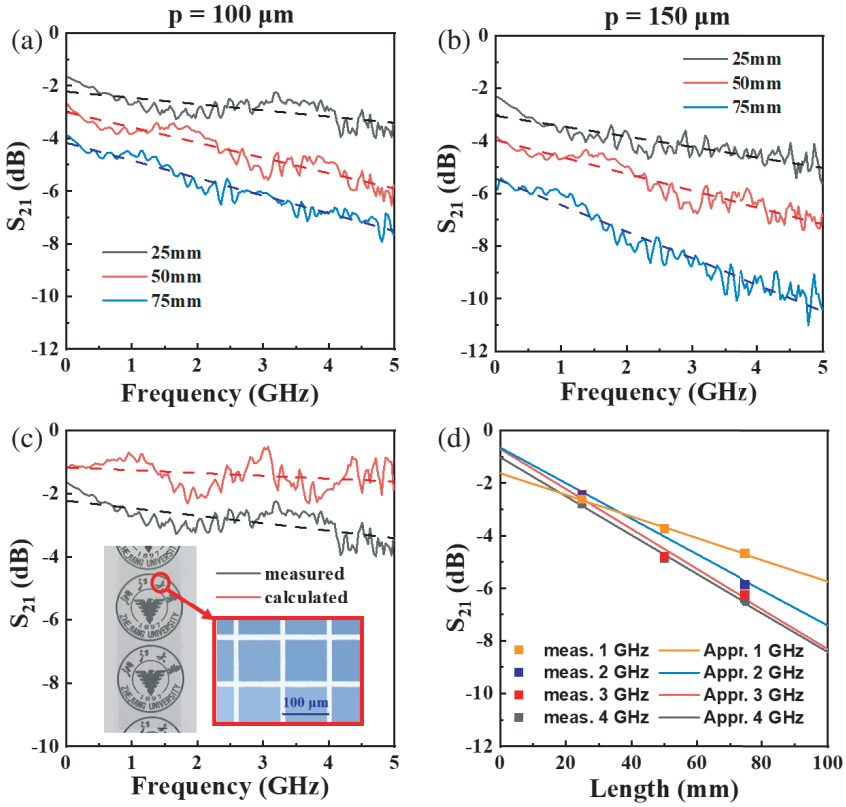

Figure 3. Measured S_{21} spectra as functions of the lengths of our transparent CPWs based on Ag μ-MMs with (a) $p = 100\,\mu m$ and (b) 150 μm. (c) Measured (black) and calculated (red) S_{21} spectra of our transparent CPW with $L = 25\,mm$ and $p = 100\,\mu m$. The calculated S_{21} spectrum is obtained through the S_{21} spectrum of the 75-mm long CPW minus the spectrum of the 50-mm long CPW according to Eq. (2). Inset is a photo of our transparent CPW with $L = 25\,mm$ and $p = 100\,\mu m$. The curves in (a)–(c) are approximated with the dashed lines to guide the eye. (d) Measured S_{21} values (dots) and their fitting lines of our transparent CPWs with $p = 100\,\mu m$ and $L = 25$, 50, and 75 mm at 1, 2, 3, and 4 GHz.

losses of the CPWs with $p = 100\,\mu m$ are about 0.24, 0.58 and 0.67 dB/GHz, respectively (Fig. 3(a)) and those of CPWs with $p = 150\,\mu m$ are about 0.40, 0.64 and 1.01 dB/GHz, respectively (Fig. 3(b)). This indicates that the longer CPW has larger insertion loss. Because of the better conductivity of the dense Ag μ-MM than that of the spare one (Fig. 2(d)), the CPWs based on the latter are more lossy (Figs. 3(a) and 3(b)).

To reduce the impact of the connections between the SMA connectors and the CPWs on the measured S_{21}, we performed the following calculation [10]:

$$S_{21}^{L_{c,c}} = S_{21}^{L_{a,m}} - S_{21}^{L_{b,m}} \tag{3}$$

where $S_{21}^{L_{a,m}}$ and $S_{21}^{L_{b,m}}$ are the measured S_{21} values of CPWs with lengths of L_a and L_b; $S_{21}^{L_{c,c}}$ is the calculated S_{21} value of CPW with a length of L_c; and $L_c = L_a - L_b$ holds. Assuming that the coupling losses induced by the SMA connections are all the same, the calculated $S_{21}^{L_{c,c}}$ means the pure insertion loss of the CPW with length L_c, which does not include the coupling losses of the two ends. For example, taking $L_a = 75\,mm$ and $L_b = 50\,mm$, we calculated $S_{21}^{L_{c,c}}$ of the 25-mm long CPW based on the dense Ag μ-MM with $p = 100\,\mu m$ and plotted it in Fig. 3(c), where the measured spectrum is also presented for comparison. From Fig. 3(c), it is seen that the pure insertion loss of the 25-mm long CPW is only 0.09 dB/GHz, much smaller than that of the measured result (0.24 dB/GHz). The difference between them is the coupling losses at the two ends.

In order to quantitatively analyze the coupling loss and the propagation loss of the EM wave, the measured S_{21}'s of CPWs with the three lengths were extracted at 1, 2, 3, and 4 GHz, respectively and plotted in Fig. 3(d). Here only the CPWs based on the dense mesh were taken as an example for analysis. At each frequency, the measured S_{21}'s are fitted with a straight line. The intersection of the line with the vertical axis means the coupling loss of the CPW to the SMA connectors, while the slope represents the propagation loss. This is the so-called cut-off method, where the coupling losses of CPWs with different lengths are assumed to be the same. From this method, we obtained the coupling losses and propagation losses of the meshed CPW at different frequencies, summarized in Table 2. The correlation coefficients, $R2$, of fitting lines are all greater than 0.97, indicating a good fitting degree. From Table 2, it is seen that the propagation loss of CPW increases with frequency. They are all smaller than 0.1 dB/mm. When multiplied by 25 mm, they match well with the calculated S_{21}'s values shown in Fig. 3(c). The coupling loss varies with frequency irregularly. If further assuming the same coupling statuses at the two ends of the CPW, the coupling loss at a single end will be well below 1 dB. In this case, it can be predicted that the CPW used in the antenna will introduce an insertion loss of only about 2 dB, comparable to that of a reported transparent CPW [33]. This CPW provides a good feed to the antenna, allowing a high radiation efficiency of our antenna superior to those of the transparent antennas reported previously as compared in Table 3 below.

Table 2. Losses of our transparent CPW based on the dense Ag μ-MM with $p = 100\,\mu m$ extracted from the cut-off method.

Frequency (GHz)	Coupling Loss (dB)	Propagation Loss (dB/mm)	$R2$
1	1.62	0.041	0.997
2	0.65	0.068	0.978
3	0.70	0.074	0.982
4	1.02	0.076	0.996

Based on the Ag μ-MM with $p = 100\,\mu m$ and $t = 190\,nm$, we fabricated a transparent antenna according to the design shown in Fig. 1(a) and demonstrated it in Fig. 4(a). No existing MM-based transparent antennas are thinner than ours. The sectorial mesh in the patch region (inset of Fig. 1(a)) has the same horizontal period, i.e., $p = 100\,\mu m$. For comparison, an opaque antenna based on a solid Ag film with the same thickness was also fabricated and demonstrated in Fig. 4(b). The university logos

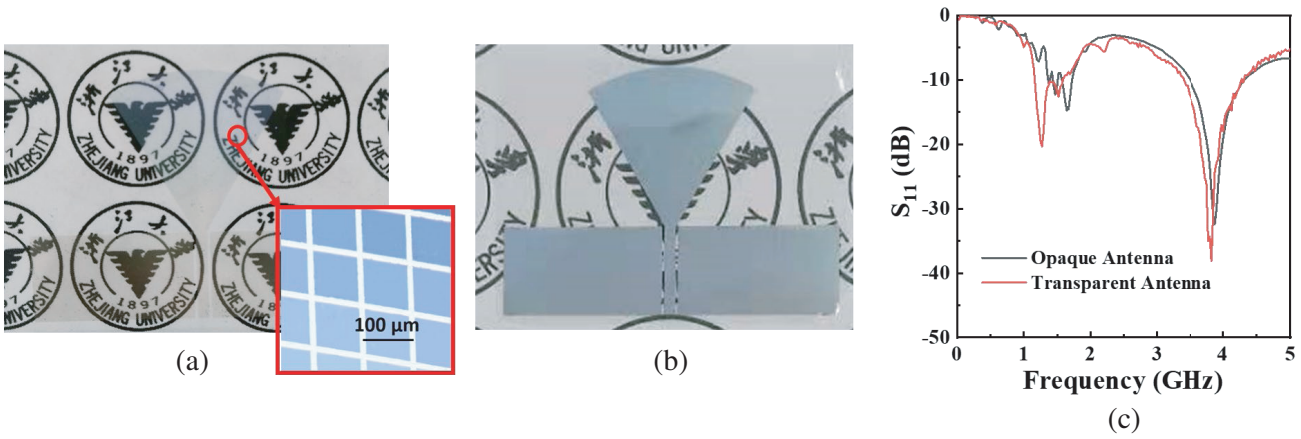

Figure 4. Photographs of the fabricated (a) transparent antenna based on the Ag μ-MM with $p = 100\,\mu m$ and $t = 190\,nm$ (inset: microscopic image of the Ag μ-MM), and (b) opaque antenna based on the solid Ag film with the same thickness. The diameters of the logos of Zhejiang University are 2.2 cm in (a) and 4.5 cm in (b). (c) Measured S_{11} spectra for both the transparent and opaque antennas.

under the meshed antenna can be clearly seen (Fig. 4(a)), while those under the unmeshed antenna are hardly seen because the 190-nm thick solid Ag film totally blocks the light (Fig. 4(b)). The measured S_{11} spectra of these two antennas are shown in Fig. 4(c). Both antennas have very close S_{11} spectra, meaning similar return losses. This indicates that the Ag μ-MM is as effective as its film counterpart for constructing antennas. For each antenna, there are two frequency bands for $S_{11} < -10$ dB. The upper frequency band is the main operating band, which is 3.4–4.25 GHz for our transparent antenna and 3.51–4.3 GHz for the opaque one, corresponding to the fractional bandwidths of 22% and 20%, respectively. The transparent antenna working at this band has the smallest S_{11} approaching −40 dB and is promising to be applied to 5G systems. The lower frequency band is 1.16–1.58 GHz for our transparent antenna and 1.58–1.72 GHz for the opaque one, corresponding to the fractional bandwidths of 30.7% and 8.5%, respectively. The transparent antenna working at this band can be potentially applied to mobile phones and the internet of things. However, its minimal S_{11} is as large as −20 dB, meaning a lager return loss. The bandwidth of the main operating band can be widened further but it is not done intentionally because it is not the focus of this work.

3.3. Good Mechanical Flexibility of Transparent CPW and Transparent Antenna

The mechanism flexibility of the transparent CPW and transparent antenna based on Ag μ-MMs with $p = 100$ μm and $t = 190$ nm was measured using the setup shown in the inset of Fig. 5(a). The sample was clamped by two supports. One is fixed and the other is moving. By changing the movable support to a proper position, the sample can be bent at a curvature radius of about 6 mm. After being repeatedly bent 500 times, the measured S_{21} spectrum of the transparent CPW still keeps very high, less than 1 dB below the initial spectrum at most frequencies, as shown in Fig. 5(a). For the transparent antenna, the measured S_{11} spectra are almost the same before and after bending 500 cycles (Fig. 5(b)). This fully proves the excellent mechanical flexibility of our transparent antenna, which is very tolerant to the relatively poorer mechanical property of the component CPW.

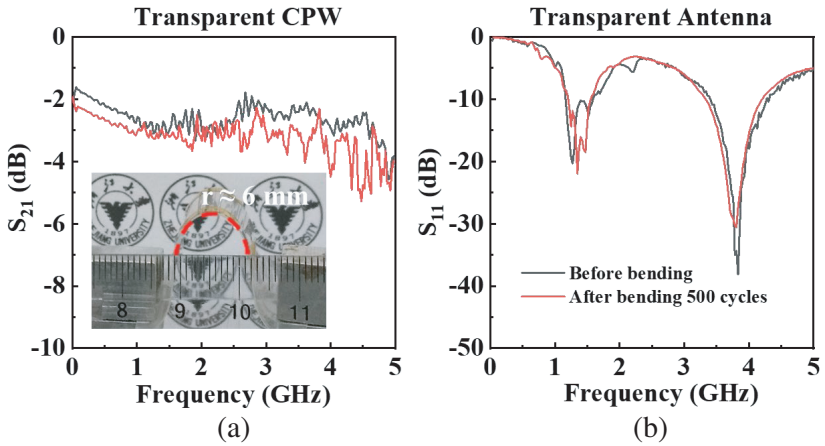

Figure 5. (a) Measured S_{21} spectra of our transparent CPW with $p = 100$ μm, $t = 190$ nm and $L = 25$ mm before and after bending 500 cycles under a curvature radius of approximately 6 mm (inset: flexibility test setup). (b) Measured S_{11} spectra of our transparent antenna with $p = 100$ μm and $t = 190$ nm before and after bending 500 cycles under the same bending radius.

3.4. Numerical Simulation of Transparent Antenna

Due to the lack of the facility, we could not do more characterizations. Instead, numerical simulations were performed to demonstrate the radiation properties of our transparent antenna. The simulation details are described in Section 2. Fig. 6(a) shows the simulated and measured S_{11} spectra of our transparent antenna. For $S_{11} < -10$ dB, the main upper frequency band of 3.0–3.9 GHz red shifts a little bit compared to the measured upper frequency band. The simulated operating frequency where

Table 3. Comprehensive comparison of our transparent antenna with various previously-reported transparent antennas.

Refs.	TCFs for transparent antennas	t_{TCF} (μm)	R_{sh} (Ω/sq)	T_{ave} (%)	Physical size (mm^2) (Electrical size (λ_0^2))	Efficiency (%)	Peak Gain	Flexibility[a]
[5]	ITO	0.4	8.68	> 80	0.209×0.433 (0.53×1.09)	49.45 (750 GHz)	3.35 dB (732 GHz)	No
[5]	FTO	0.4	14.97	> 80	0.209×0.433 (0.53×1.09)	7.78 (750 GHz)	2.26 dB (801 GHz)	No
[7]	FTO/ITO	1.4	4	> 75	29×50 (0.68×1.17)	60 (7 GHz; sim.)	2 dBi (7 GHz)	No
[11]	IZTO/Ag /IZTO	0.1	2.52	68.63	50×50 (0.41×0.41)	7.76 (2.45 GHz)	−4.23 dB (2.45 GHz)	No
[11]	μ-MM	5	0.18	62.1	50×50 (0.41×0.41)	42.69 (2.45 GHz)	2.63 dB (2.45 GHz)	No
[15]	AgHT-8	175	8	> 80	36×39 (-)	-	−3.25 dBi (2.45 GHz); −4.53 dBi (5.8 GHz)	-
[17]	Polyaniline	100	16.7	-	5×12.5 (0.16×0.40)	56 (9.7 GHz)	1.88 dBi (9.7 GHz)	No
[19]	3-layer graphene		80	90.1	10×6 (0.33×0.20)	52.5 (9.8 GHz)	0.3 dBi (8.5 GHz)	No
[23]	Ag NW network	0.237	8.5	85	-	51.7 (2.4 GHz)	-	Yes
[24]	Wavy Ag NW Network	-	< 3.8	~ 80	-	31.67 (2.3 GHz)	3.55 dBi (2.3 GHz)	Yes
[28]	Wired-MM (single-layer)	57	0.1	72	50×58 (0.67×0.77)	37 (2.43 GHz); 44 (5.15 GHz)	2.2 dBi (2.43 GHz); 3.02 dBi (5.15 GHz)	Yes
[28]	Wired-MM (double-layer)	114	-	52	50×58 (0.67×0.77)	48 (2.51 GHz); 46 (4.9 GHz)	3.2 dBi (2.51 GHz); 3.5 dBi (4.9 GHz)	Yes
[29]	Wired-MM (single-layer)	57	0.7	70	55×60 (0.45×0.49)	30 (2.45 GHz)	1.8 dBi (2.45 GHz)	Yes; r_{20}; 50 cycles
[31]	μ-MM	6.005	0.054	51.6–70.7	300×300 (2×2)	60	5.4 dBi (1.92 GHz); 5.5 dBi (2.05 GHz); 5.2 dBi (2.17 GHz)	No
[32]	μ-MM	1.01	0.44	83	2.3×2.3 (0.41×0.41)	-	2.95 dBi (54.1 GHz)	No
[33]	μ-MM	5	0.05	> 75	40×40 (-)	43 (2.44 GHz); 46 (5.5 GHz)	0.74 dBi (2.44 GHz); 2.3 dBi (5.5 GHz)	No
[34]	μ-MM	~ 100	0.5	70	100×100 (0.88×0.88)	75 (2.4–2.9 GHz)	5–6.4 dBi (2.4–2.9 GHz)	-
[36]	μ-MM	5	0.04	70.2	Patch: 105×290 (0.22×0.60); Dipole: 40×210 (0.08×0.43)	Patch: 83.8; Dipole: 72.1 (470–771 MHz)	Patch: 6.2 dBi; Dipole: 2.4 dBi (470–771 MHz)	No
[37]	μ-MM	5.5	0.02	60	40×40 (0.47×0.47)	70 (3.55 GHz)	4.6 dBi (3.55 GHz)	No
[38]	μ-MM	5	0.1	93	60×60 (0.94×0.94)	85 (4.7 GHz)	3.8 dBi (4.7 GHz)	Yes
[38]	μ-MM	5	0.1	86	22.5×45 (1.95×3.9)	61 (26 GHz)	9.7 dBi (26 GHz)	Yes; $\omega_{2.3}$
This work	**μ-MM**	**0.19**	**1.75**	**83.1**	**59.9×43.535 (0.76 × 0.56)**	**89.7 (3.45 GHz, sim.)**	**3.03 dBi (3.45 GHz, sim.)**	**Yes; r_6; 500 cycles**

[a] r_{20} and r_6 represent the bending radii of 20 and 6 mm, respectively. $\omega_{2.3}$ represents the bending radian angle of 2.3.

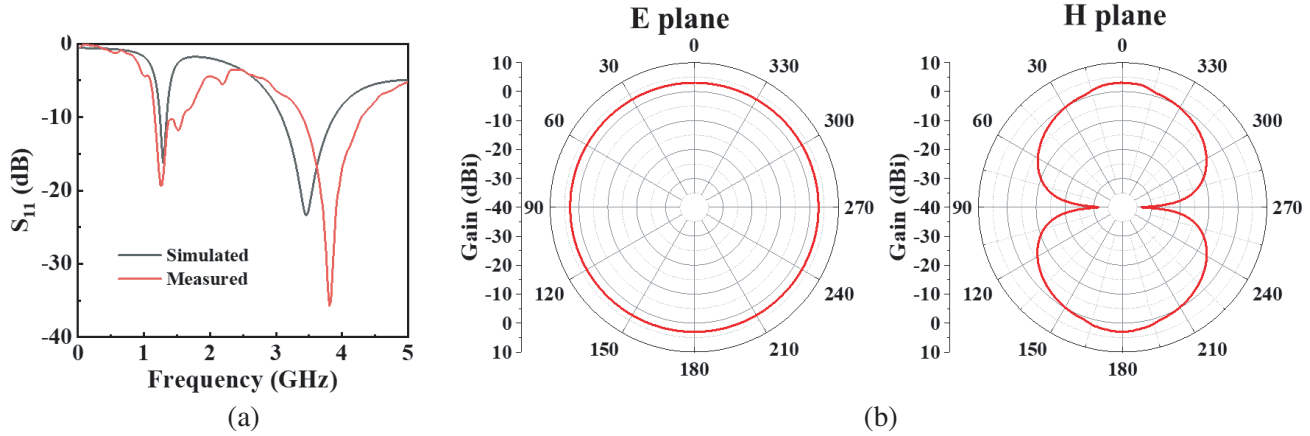

Figure 6. (a) Simulated and measured S_{11}, (b) simulated two-dimensional radiation patterns at 3.45 GHz at the E and H planes of the proposed transparent antenna.

S_{11} reaches minimum is 3.45 GHz, merely 0.35 GHz smaller than the measured one. One reason for the deviation is probably the PE substrate used in our experiment, which may have a smaller dielectric constant, leading to a reduced patch capacitance. Another reason may be the SMA connector used for EM characterization, introducing a parallel capacitance and thus a decrease of the total capacitance of the whole device. Fortunately, these effects are not that significant, and the deviation between the measured and simulated results is well acceptable, fully verifying the numerical simulation accuracy.

Based on the numerical model, the radiation properties of our transparent antenna at 3.45 GHz are evaluated. From Fig. 6(b), an omnidirectional radiation pattern is clearly observed. The radiation efficiency is 89.7% and the peak gain is 3.03 dBi at 3.45 GHz, due to the high conductivity of the Ag μ-MM. To the best of our knowledge, it is the first time to report the sub-micron thick μ-MM-based high-efficiency transparent and flexible wideband antenna. Despite the thin μ-MM, the comprehensive optical, electromagnetic, and mechanical properties of our antenna are still comparable and even superior to those of previously-reported transparent antennas [5, 7, 11, 15, 17, 19, 23, 24, 28, 29, 31–34, 36–38], as listed in Table 3.

4. CONCLUSION

In conclusion, an optically transparent and mechanically flexible wideband antenna consisting of a fan-shaped patch fed with a CPW has been first demonstrated experimentally based on an Ag μ-MM with the thickness of only 190 nm. The Ag μ-MM has visible transmittance as high as 83.1% and sheet resistance as low as 1.75 Ω/sq, allowing for the low-loss transparent CPW and transparent antenna. Systematic characterizations and analyses show that the Ag μ-MM based transparent CPW is a good feed to the antenna. The measured S_{11} spectrum of the transparent antenna matches well with that of the opaque counterpart, confirming that the Ag μ-MM is a good replacement of the Ag film for antennas. The measured fractional bandwidth of our transparent antenna is 22% from 3.4 to 4.25 GHz, consistent with the simulated results. Based on the accurate numerical model, the radiation efficiency up to 89.7% and the peak gain up to 3.03 dBi are calculated at 3.45 GHz, mainly attributed to the high conductivity of the Ag μ-MM. In general, despite the sub-micron thick μ-MM, the transparency, radiation efficiency, and mechanical properties of our transparent antenna are obviously superior to those of the transparent antennas reported previously, and the overall size and radiation gain are also comparable. Therefore, our transparent antenna has an excellent comprehensive performance, which is of great potential for practical applications including applications in the emerging field of flexible and wearable electronics.

REFERENCES

1. Simons, R. N. and R. Q. Lee, "Feasibility study of optically transparent microstrip patch antenna," *IEEE Antennas and Propagation Society International Symposium*, Montreal, Quebec, Canada, Jul. 13–18, 1997.
2. Syed Feroze Hussain, S. and D. Thiripurasundari, "A review on optically transparent antenna fabricated with conductive nano-material oxides," *J. Electron. Mater.*, Sep. 2022, https://doi.org/10.1007/s11664-022-09916-w.
3. Sayem, A. S. M., A. Lalbakhsh, K. P. Esselle, J. L. Buckley, B. O'Flynn, and R. B. V. B. Simorangkir, "Flexible transparent antennas: Advancements, challenges, and prospects," *IEEE Open J. Antennas Propag.*, Vol. 3, 1109–1133, Sep. 2022.
4. Lee, S. Y., M. Choo, S. Jung, and W. Hong, "Optically transparent nano-patterned antennas: A review and future directions," *Appl. Sci. — Basel*, Vol. 8, No. 6, 901, May 2018.
5. Thampy, A. S. and S. K. Dhamodharan, "Performance analysis and comparison of ITO- and FTO-based optically transparent terahertz U-shaped patch antennas," *Physica E*, Vol. 66, 52–58, Feb. 2015.
6. So, K. K., B.-J. Chen, and C. H. Chan, "Microwave and millimeter-wave MIMO antenna using conductive ITO film," *IEEE Access*, Vol. 8, 207024–207033, Nov. 2020.
7. Potti, D., Y. Tusharika, M. G. N. Alsath, S. Kirubaveni, M. Kanagasabai, R. Sankararajan, S. Narendhiran, and P. Balagi Bhargav, "A novel optically transparent UWB antenna for automotive MIMO communications," *IEEE Trans. Antennas Propag.*, Vol. 69, No. 7, 3821–3828, Jul. 2021.
8. Green, R. B., M. Guzman, N. Izyumskaya, B. Ullah, S. Hia, J. Pitchford, R. Timsina, V. Avrutin, Ü. Özgür, H. Morkoç, N. Dhar, and E. Topsakal, "Optically transparent antennas and filters," *IEEE Antennas Propag. Mag.*, Vol. 61, No. 3, 37–47, Jun. 2019.
9. Cairns, D. R., R. P. Witte II, D. K. Sparacin, S. M. Sachsman, D. C. Paine, and G. P. Crawford, "Strain-dependent electrical resistance of tin-doped indium oxide on polymer substrates," *Appl. Phys. Lett.*, Vol. 76, No. 11, 1425–1427, Mar. 2000.
10. Colombel, F., X. Castel, M. Himdi, G. Legeay, S. Vigneron, and E. M. Cruz, "Ultrathin metal layer, ITO film and ITO/Cu/ITO multilayer towards transparent antenna," *IET Sci. Meas. Technol.*, Vol. 3, No. 3, 229–234, May 2009.
11. Hong, S., Y. Kim, and C. W. Jung, "Transparent microstrip patch antennas with multilayer and metal-mesh films," *IEEE Antennas Wirel. Propag. Lett.*, Vol. 16, 772–775, 2017.
12. Zarbakhsh, S., M. Akbari, M. Farahani, A. Ghayekhloo, T. A. Denidni, and A.-R. Sebak, "Optically transparent subarray antenna based on solar panel for CubeSat application," *IEEE Trans. Antennas Propag.*, Vol. 68, No. 1, 319–328, Jan. 2020.
13. Peter, T., R. Nilavalan, H. F. AbuTarboush, and S. W. Cheung, "A novel technique and soldering method to improve performance of transparent polymer antennas," *IEEE Antennas Wirel. Propag. Lett.*, Vol. 9, 918–921, 2010.
14. Hakimi, S., S. K. A. Rahim, M. Abedian, S. M. Noghabaei, and M. Khalily, "CPW-fed transparent antenna for extended ultrawideband applications," *IEEE Antennas Wirel. Propag. Lett.*, Vol. 13, 1251–1254, 2014.
15. Malek, M. A., S. Hakimi, S. K. A. Rahim, and A. K. Evizal, "Dual-band CPW-fed transparent antenna for active RFID tags," *IEEE Antennas Wirel. Propag. Lett.*, Vol. 14, 919–922, 2015.
16. N. J. Kirsch, N. A. Vacirca, E. E. Plowman, T. P. Kurzweg, A. K. Fontecchio, and K. R. Dandekar, "Optically transparent conductive polymer RFID meandering dipole antenna," *IEEE International Conference on RFID*, Orlando, FL, USA, Apr. 30–May 2, 2013.
17. Rmili, H., J. L. Miane, H. Zangar, and T. Olinga, "Design of microstrip-fed proximity-coupled conducting-polymer patch antenna," *Microw. Opt. Technol. Lett.*, Vol. 48, No. 4, 655–660, Apr. 2006.
18. Yin, M., L. Wu, H. Chen, X. Zhang, W. Wang, and Z. Liu, "Transparent UHF RFID tags based on CVD-grown graphene films," *Nanotechnology*, Vol. 33, No. 50, 505501, Oct. 2022.

19. Kosuga, S., S. Nagata, S. Kuromatsu, R. Suga, T. Watanabe, O. Hashimoto, and S. Koh, "Optically transparent antenna based on carrier-doped three-layer stacked graphene," *AIP Adv.*, Vol. 11, No. 3, 035136, Mar. 2021.
20. Kosuga, S., R. Suga, O. Hashimoto, and S. Koh, "Graphene-based optically transparent dipole antenna," *Appl. Phys. Lett.*, Vol. 110, No. 23, 233102, Jun. 2017.
21. Raji, A.-R. O., S. Salters, E. L. G. Samuel, Y. Zhu, V. Volman, and J. M. Tour, "Functionalized graphene nanoribbon films as a radiofrequency and optically transparent material," *ACS Appl. Mater. Interfaces*, Vol. 6, No. 19, 16661–16668, Sep. 2014.
22. Sadat, S., M. Shokooh-Saremi, M. M. Mirsalehi, and M.-M. Bagheri-Mohagheghi, "Electromagnetic characterisation of multi-wall carbon nanotube-doped fluorine tin oxide for transparent antenna applications," *IET Microw. Antennas Propag.*, Vol. 13, No. 6, 859–863, Mar. 2019.
23. Goliya, Y., A. Rivadeneyra, J. F. Salmeron, A. Albrecht, J. Mock, M. Haider, J. Russer, B. Cruz, P. Eschlwech, E. Biebl, M. Becherer, and M. R. Bobinger, "Next generation antennas based on screen-printed and transparent silver nanowire films," *Adv. Opt. Mater.*, Vol. 7, No. 21, 1900995, Aug. 2019.
24. Kim, B. S., K.-Y. Shin, J. B. Pyo, J. Lee, J. G. Son, S.-S. Lee, and J. H. Park, "Reversibly stretchable, optically transparent radio-frequency antennas based on wavy Ag nanowire networks," *ACS Appl. Mater. Interfaces*, Vol. 8, No. 4, 2582–2590, Jan. 2016.
25. Song, L., A. C. Myers, J. J. Adams, and Y. Zhu, "Stretchable and reversibly deformable radio frequency antennas based on silver nanowires," *ACS Appl. Mater. Interfaces*, Vol. 6, No. 6, 4248–4253, Mar. 2014.
26. Rai, T., P.Dantes, B.Bahreyni, and W. S. Kim, "A stretchable RF antenna with silver nanowires," *IEEE Electron Device Lett.*, Vol. 34, No. 4, 544–546, Apr. 2013.
27. Komoda, N., M. Nogi, K. Suganuma, K. Kohno, Y. Akiyama, and K. Otsuka, "Printed silver nanowire antennas with low signal loss at high-frequency radio," *Nanoscale*, Vol. 4, No. 10, 3148–3153, Mar. 2012.
28. Sayem, A. S. M., R. Simorangkir, K. P. Esselle, and R. M. Hashmi, "Development of robust transparent conformal antennas based on conductive mesh-polymer composite for unobtrusive wearable applications," *IEEE Trans. Antennas Propag.*, Vol. 67, No. 12, 7216–7224, Dec. 2019.
29. Sayem, A. S. M., K. P. Esselle, R. M. Hashmi, and H. Liu, "Experimental studies of the robustness of the conductive-mesh-polymer composite towards the development of conformal and transparent antennas," *Smart Mater. Struct.*, Vol. 29, No. 8, 085015, Aug. 2020.
30. Kang, S. H. and C. W. Jung, "Transparent patch antenna using metal mesh," *IEEE Trans. Antennas Propag.*, Vol. 66, No. 4, 2095–2100, Apr. 2018.
31. Hautcoeur, J., F. Colombel, M. Himdi, X. Castel, and E. M. Cruz, "Large and optically transparent multilayer for broadband H-shaped slot antenna," *IEEE Antennas Wirel. Propag. Lett.*, Vol. 12, 933–936, 2013.
32. Hautcoeur, J., L. Talbi, and K. Hettak, "Feasibility study of optically transparent CPW-fed monopole antenna at 60-GHz ISM bands," *IEEE Trans. Antennas Propag.*, Vol. 61, 1651–1657, Apr. 2013.
33. Li, Q. L., S. W. Cheung, D. Wu, and T. I. Yuk, "Optically transparent dual-band MIMO antenna using micro-metal mesh conductive film for WLAN system," *IEEE Antennas Wirel. Propag. Lett.*, Vol. 16, 920–923, 2017.
34. Ding, C., L. Liu, and K.-M. Luk, "An optically transparent dual-polarized stacked patch antenna with metal-mesh films," *IEEE Antennas Wirel. Propag. Lett.*, Vol. 18, No. 10, 1981–1985, Oct. 2019.
35. Zhang, Y., S. Shen, C. Chiu, and R. Murch, "Hybrid RF-solar energy harvesting systems utilizing transparent multiport micromeshed antennas," *IEEE Trans. Microw. Theory Tech.*, Vol. 67, No. 11, 4534–4546, Nov. 2019.
36. Tung, P. D. and C. W. Jung, "Optically transparent wideband dipole and patch external antennas using metal mesh for UHD TV applications," *IEEE Trans. Antennas Propag.*, Vol. 68, No. 3, 1907–1917, Mar. 2020.

37. Hu, H.-T., B.-J. Chen, and C. H. Chan, "A transparent proximity-coupled-fed patch antenna with enhanced bandwidth and filtering response," *IEEE Access*, Vol. 9, 32774–32780, Feb. 2021.
38. Qiu, H., H. Liu, X. Jia, Z.-Y. Jiang, Y.-H. Liu, J. Xu, T. Lu, M. Shao, T.-L. Ren, and K. J. Chen, "Compact, flexible, and transparent antennas based on embedded metallic mesh for wearable devices in 5G wireless network," *IEEE Trans. Antennas Propag.*, Vol. 69, No. 4, 1864–1873, Apr. 2021.
39. Viti, L., J. Hu, D. Coquillat, W. Knap, A. Tredicucci, A. Politano, and M. S. Vitiello, "Black phosphorus terahertz photodetectors," *Adv. Mater.*, Vol. 27, No. 37, 5567–5572, Aug. 2015.
40. Viti, L., A. Politano, K. Zhang, and M. S. Vitiello, "Thermoelectric terahertz photodetectors based on selenium-doped black phosphorus flakes," *Nanoscale*, Vol. 11, No. 4, 1995–2002, Jan. 2019.
41. Wang, L., L. Han, W. Guo, L. Zhang, C. Yao, Z. Chen, Y. Chen, C. Guo, K. Zhang, C. Kuo, C. S. Lue, A. Politano, H. Xing, M. Jiang, X. Yu, X. Chen, and W. Lu, "Hybrid Dirac semimetal-based photodetector with efficient low-energy photon harvesting," *Light-Sci. Appl.*, Vol. 11, No. 1, 53, Mar. 2022.
42. Guo, C., W. Guo, H. Xu, L. Zhang, G. Chen, G. D'Olimpio, C. Kuo, C. S. Lue, L. Wang, A. Politano, X. Chen, and W. Lu, "Ultrasensitive ambient-stable $SnSe_2$-based broadband photodetectors for room-temperature IR/THz energy conversion and imaging," *2D Mater.*, Vol. 7, No. 3, 035026, Jun. 2020.
43. Liu, C., L. Wang, X. Chen, A. Politano, D. Wei, G. Chen, W. Tang, W. Lu, and A. Tredicucci, "Room-temperature high-gain long-wavelength photodetector via optical-electrical controlling of hot carriers in graphene," *Adv. Opt. Mater.*, Vol. 6, No. 24, 1800836, Dec. 2018.
44. Viti, L., J. Hu, D. Coquillat, A. Politano, C. Consejo, W. Knap, and M. S. Vitiello, "Heterostructured hBN-BP-hBN nanodetectors at terahertz frequencies," *Adv. Mater.*, Vol. 28, No. 34, 7390–7396, Sep. 2016.
45. Xu, H., C. Guo, J. Zhang, W. Guo, C. Kuo, C. S. Lue, W. Hu, L. Wang, G. Chen, A. Politano, X. Chen, and W. Lu, "$PtTe_2$-based type — II Dirac semimetal and its van der Waals heterostructure for sensitive room temperature terahertz photodetection," *Small*, Vol. 15, No. 52, 1903362, Dec. 2019.